

Simultaneous emission from dust and gas in the planetary debris orbiting a white dwarf

Laura K. Rogers,¹★ Christopher J. Manser,^{2,3} Amy Bonsor,¹ Erik Dennihy,⁴ Simon Hodgkin,¹ Markus Kissler-Patig,⁵ Samuel Lai,⁶ Carl Melis,⁷ Siyi Xu (许偲艺),⁸ Nicola Gentile Fusillo,⁹ Boris Gänsicke,³ Andrew Swan,³ Odette Toloza,^{10,11} Dimitri Veras^{3,12,13}

¹ *Institute of Astronomy, University of Cambridge, Madingley Road, Cambridge CB3 0HA, UK*

² *Astrophysics Group, Department of Physics, Imperial College London, Prince Consort Road, London, SW7 2AZ, UK*

³ *Department of Physics, University of Warwick, Coventry CV4 7AL, UK*

⁴ *Rubin Observatory Project Office, 950 N. Cherry Ave., Tucson, AZ 85719, USA*

⁵ *European Space Agency - European Space Astronomy Centre, Camino Bajo del Castillo, s/n., 28692 Villanueva de la Canada, Madrid, Spain*

⁶ *Commonwealth Scientific and Industrial Research Organisation (CSIRO), Space & Astronomy, P. O. Box 1130, Bentley, WA 6102, Australia*

⁷ *Center for Astrophysics and Space Sciences, University of California, San Diego, CA 92093-0424, USA*

⁸ *Gemini Observatory, 670 N. A'ohoku Place, Hilo, HI 96720, USA*

⁹ *Department of Physics, Università degli Studi di Trieste, Via A. Valerio 2, 34127, Trieste, Italy*

¹⁰ *Departamento de Física, Universidad Técnica Federico Santa María, Avenida España 1680, Valparaíso, Chile*

¹¹ *Millennium Nucleus for Planet Formation, NPF, Valparaíso, Av. España 1680, Chile*

¹² *Centre for Exoplanets and Habitability, University of Warwick, Coventry CV4 7AL, UK*

¹³ *Centre for Space Domain Awareness, University of Warwick, Coventry CV4 7AL, UK*

Accepted XXX. Received YYY; in original form ZZZ

ABSTRACT

There is increasing evidence for the presence and variability of circumstellar dust and gas around white dwarfs that are polluted with exoplanetary material, although the origin of this dust and gas remains debated. This paper presents the first near-simultaneous observations of both circumstellar dust (via broadband emission) and gas (via emission lines) around a polluted white dwarf. From the optical spectra the gaseous emission lines, notably the calcium infrared triplet and magnesium lines, show significant increases and decreases in their strength over timescales of weeks, while the oxygen and iron lines remain relatively stable. Near-infrared *JHKs* photometry reveals dust emission changes of up to 0.2 magnitudes in the *Ks* band over similar timescales, marking the shortest variability timescales observed to date. The two epochs with the strongest emission were correlated between the dust (*Ks* band brightening) and gas (strengthened calcium and magnesium lines), showing for the first time that the dust and gas must be produced near-simultaneously with a common origin, likely in collisions.

Key words: white dwarfs – circumstellar matter – planetary systems – stars: individual: WD J210034.65+212256.89

1 INTRODUCTION

There is strong observational evidence for planetary systems around white dwarf stars. Between 25–50 per cent of single white dwarfs are polluted with heavy elements (> He) resulting from the accretion of planetary material (Zuckerman et al. 2003, 2010; Koester et al. 2014; Wilson et al. 2019). 1.5–4 per cent of white dwarfs show an infrared excess from warm (~1000 K) dust (e.g. Becklin et al. 2005; Kilic et al. 2006; Jura et al. 2007; Rebassa-Mansergas et al. 2019; Wilson et al. 2019; Xu et al. 2020; Lai et al. 2021). 0.067 per cent of white dwarfs are expected to show Ca II emission lines from a Keplerian rotating gas disc (Manser et al. 2020), with 21 identified to date (Gänsicke et al. 2006, 2007, 2008; Melis et al. 2010; Farihi et al. 2012; Melis et al. 2012; Brinkworth et al. 2012;

Dennihy et al. 2020; Melis et al. 2020; Gentile Fusillo et al. 2021), and a handful of white dwarfs show absorption from circumstellar gas (e.g. Debes et al. 2012; Xu et al. 2016). X-ray emission has been detected around one polluted white dwarf with a disc, providing direct evidence of ongoing accretion from the disc (Cunningham et al. 2022). Additionally, a few exoplanets have been discovered around white dwarfs adding to the significant observational evidence of the survival of planetary systems to the white dwarf phase (e.g. Gänsicke et al. 2019; Vanderburg et al. 2020; Blackman et al. 2021). *JWST* is expected to drastically increase this number (Limbach et al. 2022; Poulsen et al. 2024) with three candidate giant planets already identified (Limbach et al. 2024; Mullally et al. 2024).

The material polluting white dwarfs is thought to be from the scattering of planetesimals onto star-grazing orbits by outer planetary-mass perturbers (e.g. Debes & Sigurdsson 2002). The planetesimals tidally disrupt at the Roche radius and form an eccentric stream of dust

★ E-mail: laura.rogers@ast.cam.ac.uk

before they circularise, sublimate, and finally accrete onto the white dwarf (e.g. Jura 2003; Brouwers et al. 2022). The abundances of the accreted material aligns with this scenario as the majority resemble bulk Earth (e.g. Jura & Young 2014). The origin of the observable circumstellar gas discs is debated. Gas produced at the sublimation radius could viscously spread outwards causing an overlap in the location of the dust and gas (Rafikov 2011; Metzger et al. 2012). An alternative explanation for gas emission is collisions between large planetesimals that are ground down into small dust within the Roche radius of the white dwarf (Jura 2008; Kenyon & Bromley 2017a,b). Observations of infrared variability in WD 0145+234 appear consistent with simple collisional cascade models (Wang et al. 2019; Swan et al. 2021, 2024).

As highlighted above, the circumstellar environments of polluted white dwarfs are known to be variable. Most polluted white dwarfs with infrared emission from a dust disc display variability in the mid-infrared (Xu & Jura 2014; Swan et al. 2019; Swan et al. 2020, 2021), however, few display variability in the near-infrared (Rogers et al. 2020). Additionally, the largest variations in the dust are found for those white dwarfs with discs that have both an observable dusty and gaseous component (Swan et al. 2020; Guidry et al. 2024). More than half of the currently known white dwarfs with gas discs in emission exhibit variation in the morphology and/or equivalent width of the gas emission lines, attributed to precession or the orbiting of planetesimals within the disc (Wilson et al. 2014, 2015; Manser et al. 2016a,b; Dennihy et al. 2018; Manser et al. 2019; Dennihy et al. 2020; Gentile Fusillo et al. 2021; Melis et al. 2020). Furthermore, observations of transiting debris around a fraction of white dwarfs show variability in the shapes, depths and timescales of the transits which can evolve on periods of days (Vanderburg et al. 2015; Gänsicke et al. 2016; Vanderbosch et al. 2021; Farihi et al. 2022).

Numerous studies have investigated dust variability and gas variability independently, however, so far these have not been studied simultaneously. This work reports the first study of a metal polluted white dwarf hosting a circumstellar disc of dust and gas, WD J210034.65+212256.89 (hereafter called: WD J2100+2122, with properties listed in Table 1), where the dust and gas emission features have been observed simultaneously. WD J2100+2122 was first identified as a white dwarf candidate in Gentile Fusillo et al. (2019), and a combination of historic photometry and new spectra revealed it had metal pollution, a circumstellar dust disc and a circumstellar gas disc (Melis et al. 2020; Dennihy et al. 2020). The abundance of the material polluting WD J2100+2122 was reported in Rogers et al. (2023) and was found to accrete material similar in composition to bulk-Earth (Rogers et al. 2024). The gas disc hosts a rich spectrum of emission features showing lines from oxygen, calcium and iron, and a circumstellar dust disc which has an infrared excess above the white dwarf photosphere significant to 7.7σ in the *K*-band. Additionally, it was demonstrated that the gas disc emission features are variable with the appearance and disappearance of the emission features over timescales of 2 months (Dennihy et al. 2020), and the sparsely sampled *WISE* infrared lightcurves were also found to vary significantly over timescales of a year. Therefore, this was selected as the most ideal target to study simultaneous variability in the dust and gas emission.

2 OBSERVATIONS AND DATA ANALYSIS

2.1 VLT X-shooter Observations

WD J2100+2122 was observed with the echelle spectrograph X-shooter (Vernet et al. 2011) on Unit Telescope 3 (UT3) of the Very

Table 1. Properties of WD J2100+2122 with astrometry from *Gaia* DR3, and effective temperature and $\log(g)$ from Rogers et al. (2023).

Gaia DR3 number	1837948790953103232
RA	21:00:34.65
DEC	+21:22:56.89
Distance (pc)	88.1 (0.4)
SpT	DAZ
Effective Temperature (K)	25565 (358)
$\log(g)$	8.10 (0.04)
Gaia <i>G</i> (mag)	15.172 (0.003)
2MASS <i>J</i> (mag)	15.789 (0.066)
2MASS <i>H</i> (mag)	15.545 (0.134)
2MASS <i>Ks</i> (mag)	14.904 (0.119)
<i>Spitzer</i> IRAC1 (μ Jy)	679.2 (34.7)
<i>Spitzer</i> IRAC2 (μ Jy)	685.3 (34.7)

Large Telescope (VLT) at Paranal Observatory, Chile between October 2019 and September 2023. X-shooter has 3 arms: UVB (3000–5595 Å), VIS (5595–10240 Å), and NIR (10240–24800 Å); the NIR has a low signal-to-noise ratio (SNR) due to the observing set-up being optimised for the UVB and VIS, therefore, the data from this arm are not used. Supplementary Table A1 reports the observations considered in this study. Observations from multiple X-shooter programs with differing observing strategies are used. For the majority of observations STARE mode was implemented, with a 1.0 and 0.9 arcsec slit width for the UVB and VIS arms, respectively, this gives a resolving power ($\lambda/\Delta\lambda$) of 5400 and 8900. These observations consisted of two exposures lasting 571 and 600 s each for the UVB and the VIS arms, respectively. For the data from programs 0109.2383.005 and 0109.2383.007, a slit width of 1.3 and 1.2 arcsec were used giving a resolving power of 4100 and 6500 in the UVB and VIS arms, with total exposure times of 2946 and 2970 s each.

The data reduction was performed using ESOREFLEX (v 2.11.3) with the X-shooter pipeline version 2.9.1 (Freudling et al. 2013) which produced flux calibrated 1D spectra. Supplementary Table A1 reports the SNR for each exposure in the UVB and VIS arms, where the SNR was calculated between the wavelength range 4000 – 5500 Å for the UVB arm and 6000 to 9000 Å for VIS arm and is > 86 and > 47 per pixel for all exposures in the UVB and VIS arms respectively.

To analyse the emission profiles of the gas, the model spectrum of WD J2100+2122 from Rogers et al. (2023) was subtracted from each X-shooter spectrum. A low order (between 2 and 5 depending on the spectral region) polynomial was fitted to the resultant continuum-subtracted spectrum to remove any deviations from zero flux. Line fluxes were then calculated from these continuum-subtracted spectra by integrating the line flux over the regions where emission is seen as has been done previously (e.g. Xu et al. 2024), the line fluxes are reported in Supplementary Table A2. As the line profiles show the characteristic double-peaked line profiles of a rotating disc of gas, the profiles were also converted into velocity space, using the rest wavelengths of the profiles obtained from the NIST database¹ and the Doppler shift formula at non-relativistic velocities. These velocities subsequently had their systemic velocity subtracted (-31.1 km/s using values from Rogers et al. 2023) such that the velocities are with respect to the white dwarf. The maximum velocities in the disc, corresponding to the Full-Width Zero Intensity (FWZI) were determined as the point where the profile reaches the continuum.

¹ https://physics.nist.gov/PhysRefData/ASD/lines_form.html

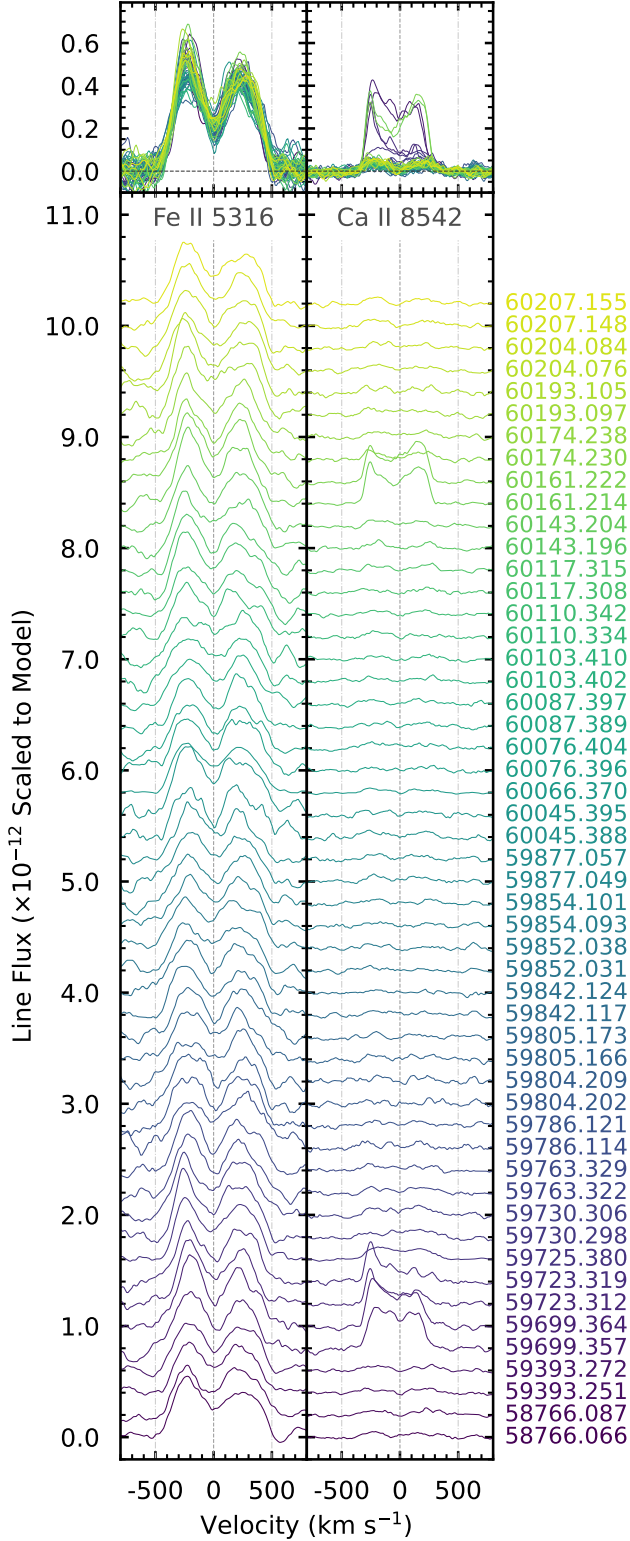


Figure 1. The evolution of the Fe II 5316 Å and Ca II 8542 Å lines over time, with each spectrum being offset vertically such that time evolves upwards and the data are labelled with their MJD. As line fluxes are used, the emission strength for each line can be compared directly. There are two regions in time in which the calcium line increases in strength, yet no increase in strength is seen in the iron line. The top panels show all the lines stacked on the same plot, showing clear differences in strengths and FWZIs.

2.2 VLT HAWK-I Observations

WDJ2100+2122 was also observed with the High Acuity Wide field K-band Imager (HAWK-I) on the Unit Telescope 4 (UT4) of the VLT (Pirard et al. 2004; Casali et al. 2006; Kissler-Patig et al. 2008; Siebenmorgen et al. 2011) between April 2022 and September 2023. Six exposures of 10 seconds were used with five dithers in a jitter box of width 20 arcseconds; this totaled five minutes of integration time per filter. The J , H , and K_s magnitudes were extracted from the phase 3 source tables and differential photometry was performed using stellar objects with K_s band magnitudes between 12 and 17 within 700 pixels of WDJ2100+2122 as comparison stars. This gave 22 sources for differential photometry in which a weighted mean was used to correct the frame-to-frame variations. The magnitude errors were calculated as a sum in quadrature of the measurement error and the systematic error calculated from the comparison stars used for differential photometry. The magnitudes and errors are reported in Supplementary Table A1, with the differential photometry giving errors of up to 0.006, 0.011, and 0.010 mags in the J , H , and K_s respectively. To test the absolute flux calibration, a comparison with 2MASS stellar sources in the field was done. The 2MASS magnitudes were transformed to match the HAWKI filters using equations from the HAWKI user manual². The standard error for the difference between the transformed 2MASS and HAWKI magnitudes are: J : 0.01 mags, H : 0.02 mags, K_s : 0.02 mags, and these should be added in quadrature with the errors reported in Supplementary Table A1 if absolutely calibrated magnitudes are required.

3 RESULTS

3.1 Gas variability

The circumstellar gas disc around WDJ2100+2122 is found to be highly variable with both emission line strength and morphological changes observed. Figure 1 illustrates the evolution of the emission line profiles for the Fe II 5316 Å and the Ca II 8542 Å lines over the four year observing period. Notably, the calcium lines exhibit two distinct epochs where the lines increase in strength significantly and decay over times of 64 and 13 d. The same behaviour is not reflected in the iron lines, which remain at a stable emission strength comparable in flux to the brightest epochs of calcium. The calcium lines show clear asymmetries during the increase in strength on 59723 MJD (and to a lesser degree 59699 MJD), whereas, during the increase in strength on 60161 MJD the calcium lines show a symmetric profile. From the top panel of Fig. 1, it is clear that the iron lines have a mostly symmetric profile throughout the observations, with the exception that there appears to be variation in the strength of the blue peak.

The top panel in Fig. 1 shows a difference in the FWZI for the iron and calcium lines, and this is quantified in Table 2. Additionally, there is a different FWZI depending on whether the calcium line is in its strong emission state versus quiescent state. Assuming a Keplerian rotating gas disc, the iron lines appear to arise from closer in to the white dwarf in comparison to the calcium lines, and when the calcium is strongly emitting, the gas appears to be originating further out than both the calcium in quiescence and the iron.

Figure 2 presents the line fluxes of the calcium, magnesium, oxygen, and iron lines. All three calcium lines demonstrate similar be-

² <https://www.eso.org/sci/software/pipelines/hawki/hawki-pipe-recipes.html>

Table 2. FWZI measurements for WD J2100+2122, where BWZI is the velocity width from the center of the emission line to the blue zero intensity, and RWZI is the same but for the red side, these velocities are related to the true velocity by $v_{\text{obs}} = v_{\text{true}} \sin i$. The orbital radii of the inner edge of the gas disc assuming an edge on inclination is also given for reference. The Fe II 5316 Å line is compared with the Ca II 8542 Å line for the strongly emitting cases (labelled ‘E’) and the quiescent case (labelled ‘Q’).

Line Å	FWZI km s ⁻¹	BWZI km s ⁻¹	r _b R _⊙	RWZI km s ⁻¹	r _r R _⊙
5316	1020 ± 7	465 ± 5	0.61 ± 0.01	555 ± 5	0.43 ± 0.01
8542 E	655 ± 7	350 ± 5	1.07 ± 0.03	305 ± 5	1.41 ± 0.05
8542 Q	795 ± 7	390 ± 5	0.87 ± 0.02	405 ± 5	0.80 ± 0.02

behaviour with both epochs of increased brightness reflected in all their line fluxes. The magnesium line shows a significant increase in brightness at the same time as the calcium lines, although in quiescence is often undetectable. In contrast, the oxygen and iron lines show some low level variability in their line fluxes, but do not exhibit the same pronounced increases in strength as the calcium lines.

3.2 Dust variability

The dust emission from WD J2100+2122 shows clear variability in the *J*, *H*, and *Ks* near-infrared bands, with certain epochs showing emission at a $> 3\sigma$ significance compared to the baseline flux level. The top panel of Fig. 3 displays the HAWKI *J*, *H* and *Ks* magnitudes plotted relative to their median values. The dashed vertical lines indicate the two epochs with the strongest emission observed for the Ca II triplet. The *Ks* band exhibits the largest variation with a change of up to 0.2 magnitudes, while the *J* and *H* bands also show variability during these epochs but at a lesser strength. It should be noted that gas emission lines can occur in the near-infrared and may be contributing to a portion of the variability (Owens et al. 2023).

There is tentative evidence for a temperature change associated with the epochs with the most significant near-infrared emission changes; these occur at 59699 and 60161 Modified Julian Dates (MJDs). The ratio of the *Ks*/*H* band fluxes shows a maximum decrease of 27 per cent whilst the *Ks*/*J* shows a maximum decrease of 32 per cent. A blackbody model was fitted to the *J*, *H* and *Ks* band excesses after subtracting off the white dwarf model flux, the median temperature and blackbody radius of the fits to the HAWKI *JHKs* photometry is 1190 K and 23.5 R_{WD} (0.29 R_⊙), with the emission peaks at 59699 and 60161 MJDs having a higher best fitting temperature of 1340 K and 1280 K respectively. However, the median error on the temperature fits is 166 K so a temperature increase in the emission peaks is not statistically significant. Further, more precise photometry extending to mid-infrared wavelengths would be required to confirm whether there is a true temperature change of the dust during these emission peaks.

3.3 Connection between gas and dust emission

Simultaneous increases and decreases in the circumstellar gas emission and infrared flux are found for WD J2100+2122. As illustrated in Fig. 3, increases in the calcium gas emission coincide with increases in the dust emission, most notable in the *Ks* band (where the infrared excess from the dust is most significant), and also reflected in the *H* and *J* bands. A Pearson’s R value of 0.8 demonstrates the strong positive correlation between the gas emission and *Ks* band

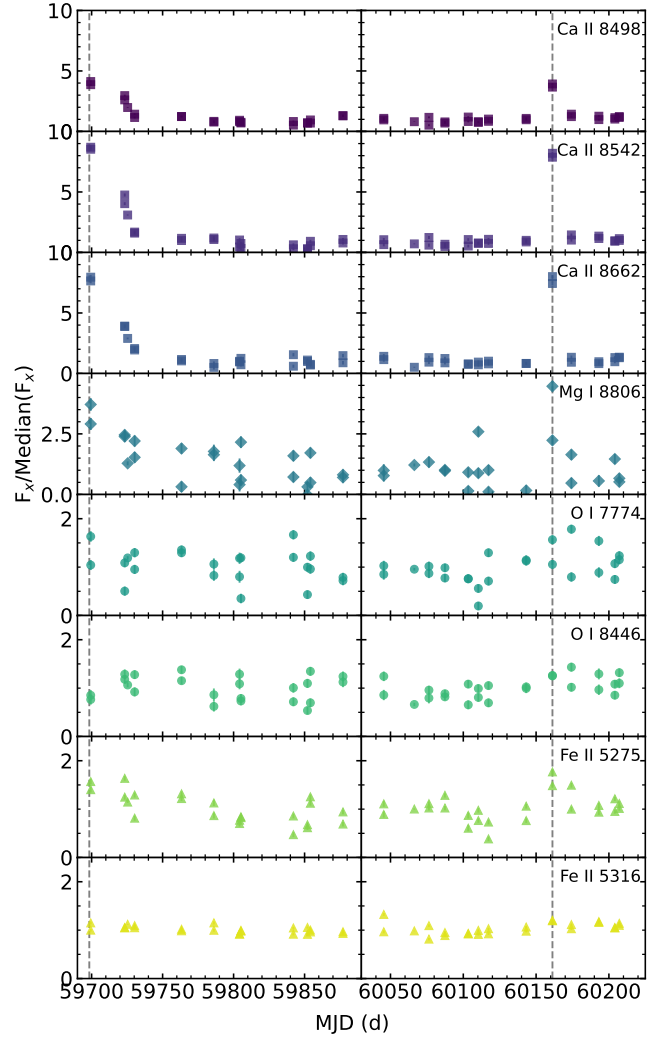


Figure 2. The line flux of the gas emission lines normalised to their median flux over time. The strong emission behaviour of the calcium lines is reflected in all 3 components of the infrared triplet and in the magnesium line, and the two strongest epochs are marked with vertical dashed lines at 59699 and 60161 MJDs. The oxygen and iron lines do not appear to vary in the same way as the calcium lines, but low level variability is clear. Error bars are plotted but are mostly hidden below the data points.

dust emission. During the two epochs which show concurrent emission, the near-infrared photometry and the optical spectroscopy were obtained on the same observing night and within a few hours of each other emphasising the simultaneity of the dust and gas emission. This correlation highlights for the first time the linked behavior of circumstellar gas and dust emission for any white dwarf.

4 DISCUSSION

This study provides for the first time clear evidence for a direct link between dust and gas production in the circumstellar disc surrounding WD J2100+2122, with two epochs showing a simultaneous strong increase in emission in both the dust and the (calcium and magnesium) gas and a subsequent return to a base quiescent level. Additionally, it was found that the dust and gas fluxes increase and decrease on timescales of days to weeks, one of the shortest ever recorded for

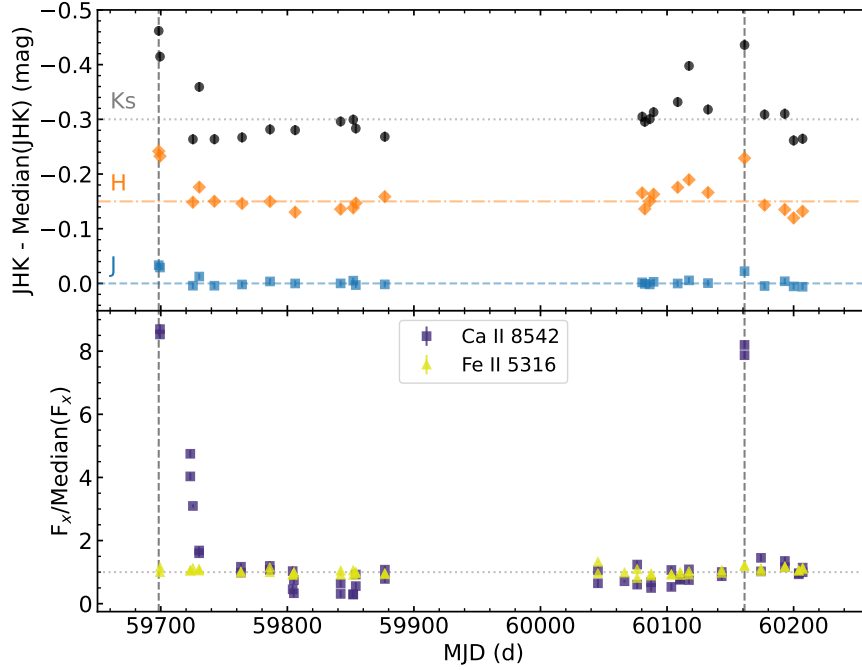


Figure 3. Top: The HAWKI J , H and K_s magnitudes plotted relative to their median magnitude and offset by 0.15 mags for clarity (horizontal lines show the median magnitude per band). Bottom: the gas emission line fluxes of one of the lines from the calcium infrared triplet (8542 Å), and one of the iron lines (5316 Å) normalised to their median flux over time (with the horizontal dotted line showing the new median flux, which as it is normalised is equal to 1). The rest of the lines are shown in Fig. 2, and data for line fluxes before this observing period are not shown here as there is no near-simultaneous near-infrared photometry. The dashed vertical lines show where there are clear correlations between the dust emission and the calcium gas emission at 59699 and 60161 MJDs.

such systems. Furthermore, the behaviour of the gas emission lines is different depending on the element, with the calcium lines showing significant line flux and morphological variations, whereas, the oxygen and iron lines remain relatively stable.

In this study simultaneous is defined as the two sets of observations taken within a few hours of one another (see Supplementary Table A1 for observing dates) which is sufficient given that the dust and gas are not thought to change on timescales less than the orbital timescale (\sim a few hours). However, as the observations were taken with a cadence of once every two weeks, it remains plausible that there is a delay of < 2 weeks between the increased dust emission and increased gas emission, and only observations with a higher cadence would be able to distinguish this.

The observations of dust and gas trace the inner regions of the circumstellar environment (< 0.01 au), however, the origin of the gas surrounding white dwarfs is debated. Following standard theories of white dwarf pollution, the circumstellar dust disc likely formed from a parent body or bodies from a distant surviving planetary system (beyond 3–5 au) which was perturbed close to the white dwarf and was tidally disrupted which then produced an infrared excess (e.g. Debes & Sigurdsson 2002; Jura 2003). However, the gas could be produced by the sublimation of the dust as it migrates inwards and/or by collisions, whether between scattered material and a pre-existing disc or through collisional cascades. There are theoretical predictions for the differences in the dust and gas emission depending on whether the gas is produced by sublimation versus collisions.

White dwarfs observed with circumstellar gas discs in emission are found to have gas and dust co-located (e.g. Melis et al. 2010). Owens et al. (2023) fitted a flat opaque dust ring as prescribed in Jura (2003) to the spectral energy distribution of WD J2100+2122 finding the inner edge of the dust to be $0.41^{+0.05}_{-0.07} R_{\odot}$, the outer edge

to be $0.70^{+0.52}_{-0.11} R_{\odot}$ (although it should be noted that the outer edge is difficult to fit for due to the lack of longer wavelength data), and the inclination to be 60^{+15}_{-35} degrees. Assuming the same inclination for the gas disc, the inner edge of the gas disc as shown by the stable iron lines (0.46 and $0.32 R_{\odot}$ for the blue and red shifted components respectively using values from Table 2) aligns with the inner edge of the dust disc measured by Owens et al. (2023). However, the inner edge of the calcium gas in emission lies further out than the dust (1.06 and $0.81 R_{\odot}$). If this additional gas emission is produced from the sublimation of the dust, it would likely be caused by the dust migrating towards the white dwarf through Poynting-Robertson (PR) drag and when hot enough, it sublimates, with the gas spreading both inwards and outwards such that it is co-located with the dust (Rafikov 2011). This would cause the gas mass to increase a time of ΔT later, associated with the PR drag timescale ($t_{PR} \approx 15$ days for $0.1 \mu\text{m}$ dust around WD J2100+2122). This is inconsistent with the observations shown here as the additional dust and gas emission during 59699 and 60161 MJDs are correlated and near-simultaneous (ΔT must be less than 2 weeks - shorter than the PR drag timescale), and the inner edge of the calcium gas during the emission peaks occurs further out than the inner edge of the dust. Therefore, it is unlikely that the additional gas emission is produced by sublimation of dust at the sublimation radius.

Instead, collisions provide a more natural explanation for the simultaneous production of dust and gas seen around WD J2100+2122. Material could be ejected from a pre-existing disc by incoming debris, or generated in destructive collisions (e.g. Malamud et al. 2021; Swan et al. 2021). Those respective scenarios would result in increased gas emission as dust sublimates above the disc’s surface, or as it is collisionally vaporised as has been observed in extreme debris discs around main sequence stars (e.g. Meng et al. 2014). Higher

cadence data around the emission peaks would be required to assess the dominant timescales for the infrared decay: settling back into an optically thick disc would happen on orbital timescales (hours), whereas collisional cascades have a characteristic $1/t$ decay (Dominik & Decin 2003). Collisions have been invoked to explain dust variability (Farihi et al. 2018; Swan et al. 2021, 2024), but this work shows for the first time that gas is likely also produced simultaneously in these collisions.

Supporting this scenario, the only white dwarfs demonstrating near-infrared *J*, *H*, or *K* band variability are those that also exhibit gas discs (Xu & Jura 2014; Xu et al. 2018; Swan et al. 2021), and Swan et al. (2020); Guidry et al. (2024) found that those white dwarfs with gas discs also show more variable mid-infrared dust emission, adding to this strong correlation between gas and dust production. Furthermore, Dennihy et al. (2017) showed that white dwarfs with gaseous discs either have the largest/brightest and/or the hottest discs, and WD J2100+2122 fits with this conclusion with the median temperature and blackbody radius for WD J2100+2122 being 1190 K and $23.5 R_{\text{WD}}$ ($0.29 R_{\odot}$).

The observed variability timescales for the gas and dust are the shortest observed to date for any planetary disc around a white dwarf, with significant *Ks* band changes detected within just one day, and the gas emission shifting between peak emission and quiescent phases within 13 days. These timescales are comparable to the photometric variability observed for white dwarfs with transiting debris which show morphological variations in these transits (Gänsicke et al. 2016; Vanderbosch et al. 2021; Farihi et al. 2022). The two observed epochs of dust and gas emission are also not identical, with the first event (beginning at 59699 MJD) showing a slower decay in the gas over 64 days compared to the 13 day decline following the peak at 60161 MJD (assuming the emission at 59699 MJD is due to a single event). The physical mechanisms responsible for the decay in the dust and gas emission must act on different timescales, highlighting the complexity of the processes at play in these dynamic circumstellar environments.

The significant variation in the strength of the calcium gas emission for WD J2100+2122 would suggest that either (i) a large amount of gaseous material is being generated somewhere in the disc at a temperature to facilitate Ca II triplet emission but not Fe II or O I emission, (ii) a region of the disc is heating to enhance Ca II triplet emission, or (iii) cooling to allow Ca III ions to recombine into Ca II (which has an ionisation energy of 11.97 eV). As the dominant source of heating for these planetary debris discs is the photoionising flux of the white dwarf, it is unlikely that options (ii) or (iii) are physical. The upper energy levels for the transitions that results in the observed emission lines are much lower for the calcium lines (3.15, 3.15, and 3.12 eV for the 8500, 8545 and 8660 Å lines respectively), in comparison to the iron lines (5.55 and 5.48 eV for 5275 and 5316 Å) and the oxygen lines (10.74 and 10.998 eV for 7774 and 8446 Å). Therefore, it is likely that scenario (i) is occurring with the gas disc surrounding WD J2100+2122 showing radially dependent excitation with an inner hotter region and an outer more dynamic cooler region. The hotter inner disc is quiescent and gives rise to the broad iron and quiescent calcium line profiles. Given the high temperature of this white dwarf the calcium is likely mostly ionised to Ca III and magnesium ionised to Mg II explaining the weak Ca II and Mg I profiles in this hot inner quiescent disc. In the outer, cooler, and more dynamic regions of the disc in which collisions are likely producing gas and dust simultaneously, the right temperature exists to facilitate these strong Ca II lines. In depth modelling of the circumstellar gas using photoionisation codes like the studies by Hartmann et al. (2011, 2014); Gänsicke et al. (2019); Steele et al. (2021); Xu et al. (2024)

will provide further insight into the composition of the gas and the variability of the different species, but is beyond the scope of this work. Additionally, the iron and quiescent calcium line profiles show a more extended red wing, compared to the calcium profile when in its strongly emitting state which has a more extended blue wing. This is likely because the disc is eccentric and non-axisymmetric; this adds to the handful of white dwarfs observed with asymmetric profiles (e.g. Melis et al. 2010). Contrasting morphologies and strengths of gaseous emission profiles for different elements has previously been observed, for example, for SDSS J1228+1040 (Manser et al. 2016a; Goksu et al. 2024). In SDSS J1228+1040 the calcium, oxygen and iron lines showed a similar spatial extent (FWZI) but differing strengths and morphologies which was explained by each element having a different intensity distribution across the disc.

5 CONCLUSIONS

This paper reports near simultaneous observations of the gas and dust surrounding the polluted white dwarf WD J2100+2122. The key conclusions are as follows:

- (i) There is a positive correlation between gas and dust emission, with the line fluxes of the calcium and magnesium gas increasing with the near-infrared photometry, representing the dust emission. This implies that there is an underlying stable gas and dust disc with additional dust and gas produced simultaneously, likely in collisions.
- (ii) The gas emission lines produced by the Ca II triplet are extremely variable and change on short timescales of days – weeks, some of the shortest variability observed in gas emission lines to date.
- (iii) The variability and behaviour of the gas emission lines depends heavily on the atomic transition observed, with line flux and morphological variations observed in the calcium lines, with limited changes in the iron and oxygen lines. There is likely radially dependent excitation, which could be caused by a hotter inner disc and a colder more dynamic outer disc.
- (iv) Observing dust and gas simultaneously is a crucial tool to disentangle models of the circumstellar environments around white dwarfs. Further studies with higher cadence around emission peaks are critical to probe the timescales on which the dust and gas evolve. The complexity of the circumstellar environment of WD J2100+2122 highlights the stochastic nature of white dwarf planetary systems and paves the way to truly understand how planetary material arrives in the atmospheres of white dwarfs.

ACKNOWLEDGEMENTS

LKR acknowledges support of an ESA Co-Sponsored Research Agreement No. 4000138341/22/NL/GLC/my = Tracing the Geology of Exoplanets and AB and LKR acknowledges support of a Royal Society University Research Fellowship, URF/R1/211421. CJM acknowledges the financial support from Imperial College London through an Imperial College Research Fellowship grant. SX is supported by the international Gemini Observatory, a program of NSF NOIRLab, which is managed by the Association of Universities for Research in Astronomy (AURA) under a cooperative agreement with the U.S. National Science Foundation, on behalf of the Gemini partnership of Argentina, Brazil, Canada, Chile, the Republic of Korea, and the United States of America. This project has received funding from the European Research Council (ERC) under the European Union’s Horizon 2020 research and innovation programme (Grant

agreement No. 101020057). The authors thank Uri Malamud for useful discussions that aided the paper. The authors also thank the referee for their helpful comments that improved the manuscript.

Based on observations collected at the European Southern Observatory under ESO programme IDs: 0103.C-0431, 0104.C-0107, 0109.C-0683(A), 0109.C-0683(B), 0109.2383.005, 0109.2383.007, 0111.C-2308(A), 0111.C-2308(B),

DATA AVAILABILITY

VLT X-shooter and VLT HAWK-I data available from the ESO archive (http://archive.eso.org/eso/eso_archive_main.html). HAWKI program IDs: 0109.C-0683(B), 0111.C-2308(B) and X-shooter program IDs: 0103.C-0431, 0104.C-0107, 0109.C-0683(A), 0109.2383.005, 0109.2383.007 and 0111.C-2308(A).

REFERENCES

- Becklin E. E., Farihi J., Jura M., Song I., Weinberger A. J., Zuckerman B., 2005, *ApJ*, **632**, L119
- Blackman J. W., et al., 2021, *Nature*, **598**, 272
- Brinkworth C. S., Gänsicke B. T., Girven J. M., Hoard D. W., Marsh T. R., Parsons S. G., Koester D., 2012, *ApJ*, **750**, 86
- Brouwers M. G., Bonsor A., Malamud U., 2022, *MNRAS*, **509**, 2404
- Casali M., et al., 2006, in McLean I. S., Iye M., eds, *Society of Photo-Optical Instrumentation Engineers (SPIE) Conference Series* Vol. 6269, *Ground-based and Airborne Instrumentation for Astronomy*. p. 62690W, doi:10.1117/12.670150
- Cunningham T., Wheatley P. J., Tremblay P.-E., Gänsicke B. T., King G. W., Toloza O., Veras D., 2022, *Nature*, **602**, 219
- Debes J. H., Sigurdsson S., 2002, *ApJ*, **572**, 556
- Debes J. H., Kilic M., Faedi F., Shkolnik E. L., Lopez-Morales M., Weinberger A. J., Slesnick C., West R. G., 2012, *ApJ*, **754**, 59
- Dennihy E., Clemens J. C., Debes J. H., Dunlap B. H., Kilkeny D., O'Brien P. C., Fuchs J. T., 2017, *ApJ*, **849**, 77
- Dennihy E., Clemens J. C., Dunlap B. H., Fanale S. M., Fuchs J. T., Hermes J. J., 2018, *ApJ*, **854**, 40
- Dennihy E., et al., 2020, *ApJ*, **905**, 5
- Dominik C., Decin G., 2003, *ApJ*, **598**, 626
- Farihi J., Gänsicke B. T., Steele P. R., Girven J., Burleigh M. R., Breedt E., Koester D., 2012, *MNRAS*, **421**, 1635
- Farihi J., et al., 2018, *MNRAS*, **481**, 2601
- Farihi J., et al., 2022, *MNRAS*, **511**, 1647
- Freudling W., Romaniello M., Bramich D. M., Ballester P., Forchi V., García-Dabó C. E., Moehler S., Neeser M. J., 2013, *A&A*, **559**, A96
- Gänsicke B. T., Marsh T. R., Southworth J., Rebassa-Mansergas A., 2006, *Science*, **314**, 1908
- Gänsicke B. T., Marsh T. R., Southworth J., 2007, *MNRAS*, **380**, L35
- Gänsicke B. T., Koester D., Marsh T. R., Rebassa-Mansergas A., Southworth J., 2008, *MNRAS*, **391**, L103
- Gänsicke B. T., et al., 2016, *ApJ*, **818**, L7
- Gänsicke B. T., Schreiber M. R., Toloza O., Gentile Fusillo N. P., Koester D., Manser C. J., 2019, *Nature*, **576**, 61
- Gentile Fusillo N. P., et al., 2019, *MNRAS*, **482**, 4570
- Gentile Fusillo N. P., et al., 2021, *MNRAS*, **504**, 2707
- Goku O. A., Kutra T., Wu Y., 2024, *AJ*, **167**, 236
- Guidry J. A., Hermes J. J., De K., Ould Rouis L. B., Ewing B. B., Kaiser B. C., 2024, *ApJ*, **972**, 126
- Hartmann S., Nagel T., Rauch T., Werner K., 2011, *A&A*, **530**, A7
- Hartmann S., Nagel T., Rauch T., Werner K., 2014, *A&A*, **571**, A44
- Jura M., 2003, *ApJ*, **584**, L91
- Jura M., 2008, *AJ*, **135**, 1785
- Jura M., Young E. D., 2014, *Annual Review of Earth and Planetary Sciences*, **42**, 45
- Jura M., Farihi J., Zuckerman B., 2007, *ApJ*, **663**, 1285
- Kenyon S. J., Bromley B. C., 2017a, *ApJ*, **844**, 116
- Kenyon S. J., Bromley B. C., 2017b, *ApJ*, **850**, 50
- Kilic M., von Hippel T., Leggett S. K., Winget D. E., 2006, *ApJ*, **646**, 474
- Kissler-Patig M., et al., 2008, *A&A*, **491**, 941
- Koester D., Gänsicke B. T., Farihi J., 2014, *A&A*, **566**, A34
- Lai S., et al., 2021, *ApJ*, **920**, 156
- Limbach M. A., Vanderburg A., Stevenson K. B., Blouin S., Morley C., Lustig-Yaeger J., Soares-Furtado M., Janson M., 2022, *MNRAS*, **517**, 2622
- Limbach M. A., et al., 2024, *ApJ*, **973**, L11
- Malamud U., Grishin E., Brouwers M., 2021, *MNRAS*, **501**, 3806
- Manser C. J., et al., 2016a, *MNRAS*, **455**, 4467
- Manser C. J., Gänsicke B. T., Koester D., Marsh T. R., Southworth J., 2016b, *MNRAS*, **462**, 1461
- Manser C. J., et al., 2019, *Science*, **364**, 66
- Manser C. J., Gänsicke B. T., Gentile Fusillo N. P., Ashley R., Breedt E., Hollands M., Izquierdo P., Pelisoli I., 2020, *MNRAS*, **493**, 2127
- Melis C., Jura M., Albert L., Klein B., Zuckerman B., 2010, *ApJ*, **722**, 1078
- Melis C., et al., 2012, *ApJ*, **751**, L4
- Melis C., Klein B., Doyle A. E., Weinberger A., Zuckerman B., Dufour P., 2020, *ApJ*, **905**, 56
- Meng H. Y. A., et al., 2014, *Science*, **345**, 1032
- Metzger B. D., Rafikov R. R., Bochkarev K. V., 2012, *MNRAS*, **423**, 505
- Mullally S. E., et al., 2024, *ApJ*, **962**, L32
- Owens D., et al., 2023, *AJ*, **166**, 5
- Pirard J.-F., et al., 2004, in Moorwood A. F. M., Iye M., eds, *Society of Photo-Optical Instrumentation Engineers (SPIE) Conference Series* Vol. 5492, *Ground-based Instrumentation for Astronomy*. pp 1763–1772, doi:10.1117/12.578293
- Poulsen S., et al., 2024, *AJ*, **167**, 257
- Rafikov R. R., 2011, *MNRAS*, **416**, L55
- Rebassa-Mansergas A., Solano E., Xu S., Rodrigo C., Jiménez-Esteban F. M., Torres S., 2019, *MNRAS*, **489**, 3990
- Rogers L. K., Xu S., Bonsor A., Hodgkin S., Su K. Y. L., von Hippel T., Jura M., 2020, *MNRAS*, **494**, 2861
- Rogers L. K., et al., 2023, *MNRAS*,
- Rogers L. K., et al., 2024, *MNRAS*,
- Siebenmorgen R., Carraro G., Valenti E., Petr-Gotzens M., Brammer G., García E., Casali M., 2011, *The Messenger*, **144**, 9
- Steele A., Debes J., Xu S., Yeh S., Dufour P., 2021, *ApJ*, **911**, 25
- Swan A., Farihi J., Wilson T. G., 2019, *MNRAS*:L, **484**, L109
- Swan A., Farihi J., Wilson T. G., Parsons S. G., 2020, *MNRAS*, **496**, 5233
- Swan A., Kenyon S. J., Farihi J., Dennihy E., Gänsicke B. T., Hermes J. J., Melis C., von Hippel T., 2021, *MNRAS*, **506**, 432
- Swan A., Farihi J., Su K. Y. L., Desch S. J., 2024, *MNRAS*, **529**, L41
- Vanderbosch Z. P., et al., 2021, *ApJ*, **917**, 41
- Vanderburg A., Johnson J. A., Rappaport S., Bieryla A., Irwin J., et al., 2015, *Nature*, **526**, 546
- Vanderburg A., et al., 2020, *Nature*, **585**, 363
- Vernet J., et al., 2011, *A&A*, **536**, A105
- Wang T.-g., et al., 2019, *ApJ*, **886**, L5
- Wilson D. J., Gänsicke B. T., Koester D., Raddi R., Breedt E., Southworth J., Parsons S. G., 2014, *MNRAS*, **445**, 1878
- Wilson D. J., Gänsicke B. T., Koester D., Toloza O., Pala A. F., Breedt E., Parsons S. G., 2015, *MNRAS*, **451**, 3237
- Wilson T. G., Farihi J., Gänsicke B. T., Swan A., 2019, *MNRAS*, **487**, 133
- Xu S., Jura M., 2014, *ApJ*, **792**, L39
- Xu S., Jura M., Dufour P., Zuckerman B., 2016, *ApJ*, **816**, L22
- Xu S., et al., 2018, *ApJ*, **866**, 108
- Xu S., Lai S., Dennihy E., 2020, *ApJ*, **902**, 127
- Xu S., et al., 2024, *AJ*, **167**, 248
- Zuckerman B., Koester D., Reid I. N., Hüensch M., 2003, *ApJ*, **596**, 477
- Zuckerman B., Melis C., Klein B., Koester D., Jura M., 2010, *ApJ*, **722**, 725

This paper has been typeset from a $\text{\TeX}/\text{\LaTeX}$ file prepared by the author.

Table A1. The dates at which X-shooter and HAWKI data were taken; if the two sets of data were taken within 4 days of each other, they are reported on the same row. The SNR for the X-shooter data is reported for both the UVB and VIS arms with each exposure reported separately if more than one is available. The HAWKI J , H and Ks magnitudes are reported with errors for differential photometry. If absolutely calibrated magnitudes are required, add the following errors in quadrature with the reported errors: J : 0.01 mags, H : 0.02 mags, Ks : 0.02 mags.

Date X-shooter	SNR UVB	SNR VIS	Date HAWKI	J (mag)	H (mag)	Ks (mag)
2019 Oct 10	152.7/159.9	84.6/89.1				
2021 June 28	149.2/161.9	82.2/87.7				
			2022 Apr 29	15.679 ± 0.006	15.604 ± 0.009	15.110 ± 0.009
2022 Apr 30	95.6/101.1	53.7/56.5	2022 Apr 30	15.684 ± 0.006	15.614 ± 0.009	15.157 ± 0.009
2022 May 24	115.9/111.2	64.1/61.5				
2022 May 26	325.6	174.5	2022 May 26	15.717 ± 0.006	15.698 ± 0.010	15.308 ± 0.009
2022 May 31	111.4/109.5	61.8/60.5	2022 May 31	15.700 ± 0.006	15.670 ± 0.009	15.212 ± 0.009
			2022 June 12	15.717 ± 0.006	15.696 ± 0.010	15.308 ± 0.009
2022 July 03	115.0/116.4	64.0/65.2	2022 July 04	15.715 ± 0.006	15.700 ± 0.010	15.305 ± 0.009
2022 July 26	88.2/93.9	49.3/52.3	2022 July 26	15.709 ± 0.006	15.696 ± 0.010	15.290 ± 0.009
2022 Aug 13	89.9/95.8	47.5/50.3				
2022 Aug 14	111.3/106.5	61.4/58.9	2022 Aug 15	15.713 ± 0.006	15.716 ± 0.010	15.291 ± 0.009
2022 Sep 20	119.7/114.1	64.7/62.5	2022 Sept 20	15.713 ± 0.006	15.710 ± 0.010	15.276 ± 0.009
2022 Sep 30	127.0/125.9	69.5/69.1	2022 Sept 30	15.708 ± 0.006	15.708 ± 0.010	15.272 ± 0.009
2022 Oct 02	114.9/113.3	62.8/62.0	2022 Oct 02	15.716 ± 0.006	15.699 ± 0.010	15.288 ± 0.009
2022 Oct 25	116.8/113.9	64.0/62.6	2022 Oct 24	15.714 ± 0.006	15.687 ± 0.010	15.303 ± 0.009
2023 Apr 11	86.0/92.4	52.0/55.8				
2023 May 02	377.7	211.1				
2023 May 12	110.9/113.0	59.9/61.3	2023 May 16	15.711 ± 0.006	15.681 ± 0.010	15.267 ± 0.009
			2023 May 18	15.713 ± 0.006	15.710 ± 0.010	15.276 ± 0.009
2023 May 23	126.9/126.8	68.7/68.5	2023 May 22	15.714 ± 0.006	15.696 ± 0.010	15.271 ± 0.009
			2023 May 25	15.710 ± 0.006	15.683 ± 0.010	15.258 ± 0.009
2023 June 08	91.5/89.2	69.6/68.2				
2023 June 15	122.6/125.0	66.7/68.2	2023 June 13	15.713 ± 0.006	15.670 ± 0.010	15.240 ± 0.009
2023 June 22	122.6/120.7	66.3/65.0	2023 June 22	15.707 ± 0.006	15.657 ± 0.009	15.174 ± 0.009
			2023 July 07	15.712 ± 0.006	15.680 ± 0.010	15.254 ± 0.009
2023 July 18	114.4/120.2	60.1/62.9				
2023 Aug 05	112.7/116.8	62.9/65.0	2023 Aug 05	15.690 ± 0.006	15.617 ± 0.009	15.136 ± 0.009
2023 Aug 18	116.9/111.0	64.0/60.8	2023 Aug 21	15.717 ± 0.006	15.703 ± 0.010	15.263 ± 0.009
2023 Sep 06	107.3/102.6	57.4/55.7	2023 Sept 06	15.709 ± 0.006	15.711 ± 0.011	15.261 ± 0.010
2023 Sep 17	122.3/123.3	66.4/67.1	2023 Sept 13	15.718 ± 0.006	15.726 ± 0.010	15.310 ± 0.010
2023 Sep 20	118.0/121.9	65.0/67.3	2023 Sept 20	15.719 ± 0.006	15.714 ± 0.010	15.307 ± 0.009

Table A2. The X-shooter line fluxes (in 10^{-13} ergs cm $^{-2}$ s $^{-1}$) for the gaseous emission lines.

MJD	Fe 5275	Fe 5316	O 7774	O 8446	Ca 8500	Ca 8545	Ca 8660	Mg 8806
58766.06648	27.8 ± 1.1	56.50 ± 0.97	9.47 ± 0.68	9.7 ± 1.0	8.64 ± 0.54	4.98 ± 0.48	4.72 ± 0.49	3.53 ± 0.34
58766.08718	39.2 ± 1.1	48.83 ± 0.92	9.72 ± 0.65	5.92 ± 0.99	8.54 ± 0.51	5.51 ± 0.46	3.28 ± 0.46	3.38 ± 0.33
59393.25132	29.0 ± 1.1	50.66 ± 0.98	4.49 ± 0.68	12.1 ± 1.0	8.85 ± 0.55	4.28 ± 0.48	6.33 ± 0.52	1.71 ± 0.36
59393.27201	23.2 ± 1.1	47.14 ± 0.90	4.09 ± 0.64	17.85 ± 0.98	10.87 ± 0.53	5.35 ± 0.45	4.71 ± 0.49	4.22 ± 0.35
59699.35677	42.2 ± 1.7	52.4 ± 1.5	15.9 ± 1.1	10.9 ± 1.4	35.51 ± 0.85	45.99 ± 0.78	36.76 ± 0.92	8.01 ± 0.56
59699.36405	47.2 ± 1.7	60.3 ± 1.4	10.1 ± 1.0	9.8 ± 1.4	37.89 ± 0.81	45.10 ± 0.74	38.26 ± 0.85	6.28 ± 0.53
59723.31152	49.2 ± 1.5	54.9 ± 1.3	10.56 ± 0.88	15.1 ± 1.1	23.97 ± 0.70	21.32 ± 0.64	18.83 ± 0.66	5.30 ± 0.47
59723.31879	37.5 ± 1.5	55.1 ± 1.3	4.89 ± 0.92	16.5 ± 1.3	27.21 ± 0.72	25.11 ± 0.67	18.67 ± 0.69	5.15 ± 0.48
59725.38037	34.44 ± 0.52	58.69 ± 0.44	11.55 ± 0.34	13.62 ± 0.60	18.17 ± 0.31	16.37 ± 0.26	13.93 ± 0.36	2.77 ± 0.18
59730.29845	38.8 ± 1.5	55.0 ± 1.3	9.25 ± 0.92	11.8 ± 1.2	10.60 ± 0.71	8.45 ± 0.66	9.91 ± 0.77	3.31 ± 0.48
59730.30573	24.4 ± 1.5	57.3 ± 1.3	12.60 ± 0.94	16.4 ± 1.2	13.13 ± 0.73	8.91 ± 0.67	9.34 ± 0.82	4.76 ± 0.49
59763.32181	36.6 ± 1.5	51.7 ± 1.3	13.15 ± 0.88	17.6 ± 1.0	11.34 ± 0.66	5.21 ± 0.62	5.57 ± 0.65	0.69 ± 0.47
59763.32908	39.6 ± 1.5	53.3 ± 1.3	12.58 ± 0.87	14.75 ± 0.98	11.29 ± 0.65	6.19 ± 0.61	5.00 ± 0.64	4.09 ± 0.46
59786.11357	33.9 ± 1.9	60.3 ± 1.6	10.3 ± 1.1	11.0 ± 1.7	7.68 ± 0.88	6.32 ± 0.81	2.44 ± 0.85	3.83 ± 0.61
59786.12085	26.0 ± 1.8	52.3 ± 1.5	8.0 ± 1.1	8.0 ± 1.4	7.12 ± 0.86	5.66 ± 0.76	3.98 ± 0.80	3.54 ± 0.57
59804.20160	21.1 ± 1.9	48.2 ± 1.6	7.8 ± 1.2	16.5 ± 1.5	7.48 ± 0.93	2.41 ± 0.85	4.59 ± 0.88	2.57 ± 0.64
59804.20890	23.2 ± 1.8	48.1 ± 1.5	11.5 ± 1.1	13.9 ± 1.4	8.51 ± 0.87	5.46 ± 0.80	4.84 ± 0.82	0.88 ± 0.61
59805.16578	25.3 ± 1.5	51.3 ± 1.3	11.56 ± 0.92	9.4 ± 1.1	6.44 ± 0.71	3.94 ± 0.67	6.01 ± 0.64	1.29 ± 0.48
59805.17305	24.8 ± 1.6	52.1 ± 1.4	3.41 ± 0.96	10.1 ± 1.1	6.95 ± 0.73	1.75 ± 0.69	3.48 ± 0.67	4.66 ± 0.50
59842.11708	25.8 ± 1.4	48.0 ± 1.2	11.66 ± 0.90	12.9 ± 1.3	7.56 ± 0.68	3.35 ± 0.62	2.89 ± 0.63	1.56 ± 0.46
59842.12435	14.2 ± 1.5	54.8 ± 1.3	16.19 ± 0.94	9.2 ± 1.2	4.82 ± 0.70	1.64 ± 0.64	7.46 ± 0.66	3.44 ± 0.48
59852.03120	20.4 ± 1.3	47.9 ± 1.2	4.19 ± 0.84	14.0 ± 1.2	6.50 ± 0.63	1.54 ± 0.58	4.77 ± 0.58	-0.04 ± 0.43
59852.03848	18.5 ± 1.4	55.3 ± 1.2	9.69 ± 0.85	6.87 ± 0.99	6.44 ± 0.64	1.57 ± 0.58	5.34 ± 0.62	0.68 ± 0.43
59854.09335	37.7 ± 1.5	52.5 ± 1.3	9.32 ± 0.95	8.9 ± 1.1	6.36 ± 0.69	2.95 ± 0.65	3.63 ± 0.68	3.70 ± 0.47
59854.10064	33.7 ± 1.5	50.5 ± 1.3	11.91 ± 0.96	17.2 ± 1.2	8.74 ± 0.70	4.88 ± 0.66	3.35 ± 0.69	1.06 ± 0.48
59877.04943	20.8 ± 1.4	50.7 ± 1.2	7.64 ± 0.93	15.9 ± 1.3	11.90 ± 0.71	5.70 ± 0.64	7.09 ± 0.67	1.52 ± 0.46
59877.05670	28.3 ± 1.5	48.8 ± 1.3	7.01 ± 0.95	14.4 ± 1.4	12.0 ± 0.85	4.15 ± 0.65	4.26 ± 0.70	1.75 ± 0.47
60045.38762	26.8 ± 1.9	50.6 ± 1.6	8.3 ± 1.1	11.0 ± 1.4	9.95 ± 0.83	5.58 ± 0.76	6.82 ± 0.93	2.14 ± 0.55
60045.39524	33.3 ± 1.8	69.4 ± 1.5	10.0 ± 1.0	15.9 ± 1.3	8.78 ± 0.77	3.42 ± 0.73	5.51 ± 0.83	1.68 ± 0.52
60066.36953	30.13 ± 0.44	51.58 ± 0.38	9.28 ± 0.27	8.48 ± 0.44	7.40 ± 0.21	3.76 ± 0.20	2.47 ± 0.21	2.63 ± 0.14
60076.39601	30.8 ± 1.5	57.3 ± 1.3	8.45 ± 0.95	10.2 ± 1.4	4.76 ± 0.75	3.20 ± 0.69	6.31 ± 0.75	-0.96 ± 0.49
60076.40363	33.5 ± 1.5	42.7 ± 1.3	9.87 ± 0.93	12.3 ± 1.1	10.72 ± 0.74	6.55 ± 0.67	4.50 ± 0.74	2.89 ± 0.48
60087.38892	38.6 ± 1.3	46.5 ± 1.1	7.51 ± 0.81	10.48 ± 0.96	6.37 ± 0.63	2.63 ± 0.60	5.96 ± 0.69	2.10 ± 0.43
60087.39656	30.8 ± 1.3	49.8 ± 1.2	9.57 ± 0.82	11.3 ± 1.0	7.27 ± 0.65	3.59 ± 0.59	4.23 ± 0.64	2.19 ± 0.43
60103.40200	26.1 ± 1.8	48.2 ± 1.6	7.39 ± 0.82	13.9 ± 1.1	10.94 ± 0.65	5.65 ± 0.59	3.62 ± 0.65	1.98 ± 0.42
60103.41000	18.2 ± 1.9	48.8 ± 1.6	7.35 ± 0.84	8.4 ± 1.2	7.58 ± 0.67	2.81 ± 0.61	3.84 ± 0.63	0.32 ± 0.43
60110.33391	29.3 ± 1.4	52.1 ± 1.2	5.43 ± 0.84	12.7 ± 1.1	7.46 ± 0.66	4.00 ± 0.61	3.45 ± 0.65	1.90 ± 0.44
60110.34153	23.0 ± 1.4	47.8 ± 1.2	1.91 ± 0.82	10.3 ± 1.1	6.85 ± 0.64	4.15 ± 0.60	4.53 ± 0.69	5.59 ± 0.43
60117.30773	11.6 ± 1.4	54.0 ± 1.2	12.58 ± 0.85	8.9 ± 1.1	7.70 ± 0.67	3.96 ± 0.62	4.90 ± 0.65	0.24 ± 0.45
60117.31535	22.0 ± 1.4	48.4 ± 1.2	6.90 ± 0.87	13.5 ± 1.0	9.40 ± 0.69	5.75 ± 0.62	3.82 ± 0.65	2.17 ± 0.45
60143.19602	31.9 ± 1.5	51.3 ± 1.3	11.12 ± 0.95	12.7 ± 1.3	8.88 ± 0.74	4.60 ± 0.68	4.00 ± 0.67	-1.12 ± 0.49
60143.20364	22.9 ± 1.4	55.7 ± 1.2	10.93 ± 0.91	13.1 ± 1.1	9.92 ± 0.72	5.30 ± 0.66	4.00 ± 0.63	0.36 ± 0.47
60161.21424	53.2 ± 1.5	62.5 ± 1.3	15.20 ± 0.90	16.1 ± 1.2	36.06 ± 0.72	43.34 ± 0.65	35.75 ± 0.64	9.63 ± 0.47
60161.22187	44.7 ± 1.4	63.1 ± 1.2	10.25 ± 0.87	16.0 ± 1.0	33.65 ± 0.67	41.62 ± 0.63	38.48 ± 0.62	4.82 ± 0.45
60174.23020	44.9 ± 1.4	53.9 ± 1.2	17.31 ± 0.89	18.3 ± 1.2	13.14 ± 0.67	7.68 ± 0.62	6.45 ± 0.68	3.55 ± 0.46
60174.23782	30.1 ± 1.5	58.4 ± 1.3	7.73 ± 0.94	13.0 ± 1.1	11.26 ± 0.71	5.41 ± 0.66	4.47 ± 0.71	1.02 ± 0.48
60193.09715	32.4 ± 1.6	61.6 ± 1.3	15.0 ± 1.0	12.4 ± 1.4	9.00 ± 0.77	7.15 ± 0.71	4.68 ± 0.75	1.21 ± 0.51
60193.10477	28.2 ± 1.6	60.7 ± 1.4	8.6 ± 1.1	16.5 ± 1.4	11.59 ± 0.82	6.10 ± 0.73	3.92 ± 0.74	-0.76 ± 0.53
60204.07595	28.6 ± 1.4	54.8 ± 1.2	10.40 ± 0.90	13.8 ± 1.1	9.38 ± 0.73	4.92 ± 0.62	4.67 ± 0.62	-1.85 ± 0.44
60204.08357	36.5 ± 1.4	55.1 ± 1.2	7.24 ± 0.89	10.9 ± 1.1	10.49 ± 0.65	5.11 ± 0.60	6.32 ± 0.62	3.16 ± 0.44
60207.14767	33.6 ± 1.4	59.8 ± 1.2	11.19 ± 0.93	14.1 ± 1.3	11.35 ± 0.67	6.04 ± 0.62	6.48 ± 0.65	1.44 ± 0.45
60207.15530	30.5 ± 1.4	57.6 ± 1.2	11.98 ± 0.90	16.9 ± 1.1	10.61 ± 0.65	5.27 ± 0.59	6.26 ± 0.62	1.13 ± 0.43